Positioning and localization of two-wavelength interferograms for wavefront reconstruction with volume holographic media

Eduardo Acedo Barbosa*

Faculdade de Tecnologia de São Paulo, CEETEPS – UNESP,
Pça Cel Fernando Prestes, 30, 01124-060, São Paulo – SP – Brazil
*ebarbosa@fatecsp.br

Abstract: This work studies both theoretically and experimentally the formation of the contour interference patterns generated by a two-wavelength real-time holographic interferometer. The resulting contour interference fringes are due to the intersection of the measured surface with parallel, equally spaced planes of constant elevation. The theoretical analysis describes how the spatial frequency of the elevation planes, their angular position, and the localization of the fringes depend on parameters of the optical setup. A theoretical model for fringe localization is developed and confirmed by the experiments, showing a strong dependence of the interferogram position on the slope of the studied surface. Due to the thick $Bi_{12}TiO_{20}$ crystal employed as the storage medium the Bragg selectivity of the holographic readout is also considered.

©2010 Optical Society of America

OCIS CODES: (090.2880) Holographic interferometry; (090.7330) Volume gratings; (120.4630) Optical inspection; (160.5320) Photorefractive materials.

References and links

1. K. Creath, *Phase Measurement Techniques: Progress in Optics*, vol. XXVI, (Elsevier Science Publishers 1988)
2. D. C. Ghiglia, G. A. Mastin, and L. A. Romero, "Cellular-automata method. for phase unwrapping," J. Opt. Soc. Am. **4**(1), 267–280 (1987).
3. A. Spik, and W. Robinson, "Investigation of the cellular automata method for phase unwrapping and its implementation on an array processor," Opt. Lasers Eng. **14**(1), 25–37 (1991).
4. M. Salvador, J. Prauzner, S. Köber, K. Meerholz, J. J. Turek, K. Jeong, and D. D. Nolte, "Three-dimensional holographic imaging of living tissue using a highly sensitive photorefractive polymer device," Opt. Express **17**(14), 11834–11849 (2009).
5. P. S. Lam, J. D. Gaskill, and J. C. Wyant, "Two-wavelength holographic interferometer," Appl. Opt. **23**(18), 3079–3081 (1984).
6. J. E. Millerd, and N. J. Brock, "Holographic profilometry with a rhodium-doped barium titanate crystal and a diode laser," Appl. Opt. **36**(11), 2427–2431 (1997).
7. E. Hack, B. Frei, R. Kästle, and U. Sennhauser, "Additive-Subtractive Two-Wavelength ESPI Contouring by Using a Synthetic Wavelength Phase Shift," Appl. Opt. **37**(13), 2591–2597 (1998).
8. E. A. Barbosa, and A. C. L. Lino, "Multiwavelength electronic speckle pattern interferometry for surface shape measurement," Appl. Opt. **46**(14), 2624–2631 (2007).
9. B. Breuckmann, and W. Thieme, "Computer-Aided Analysis of Holographic Interferograms Using the Phase-Shift Method," Appl. Opt. **24**(14), 2145–2149 (1985).
10. I. Yamaguchi, S. Ohta, and J. Kato, "Surface contouring by phase-shifting digital holography," Opt. Lasers Eng. **36**(5), 417–428 (2001).
11. G. Pedrini, P. Fröning, H. J. Tiziani, and F. M. Santoyo, "Shape measurement of microscopic structures using digital holograms," Opt. Commun. **164**(4-6), 257–268 (1999).
12. I. Balboa, H. D. Ford, and R. P. Tatam, "Low-coherence optical fibre speckle interferometry," Meas. Sci. Technol. **17**(4), 605–616 (2006).
13. E. A. Barbosa, A. A. V. Filho, M. R. R. Gesualdi, B. G. Curcio, M. Muramatsu, and D. Soga, "Single-exposure, photorefractive holographic surface contouring with multiwavelength diode lasers," J. Opt. Soc. Am. A **22**(12), 2872–2879 (2005).
14. D. Carl, M. Fratz, M. Pfeifer, D. M. Giel, and H. Höfler, "Multiwavelength digital holography with autocalibration of phase shifts and artificial wavelengths," Appl. Opt. **48**(34), H1–H8 (2009).

15. E. A. Barbosa, and J. F. Carvalho, "Surface analysis by two-diode laser photorefractive holography," Appl. Phys. B **87**(3), 417–423 (2007).
16. E. A. Barbosa, and A. O. Preto, *Optical Metrology: Optical Measurement Systems for Industrial Inspection*, Peter Lehman (Ed.) Proc. SPIE 7389 (2009).
17. E. A. Barbosa, C. B. F. de Sousa, and W. M. Maffei, "Measurement of low-derivative surface lenses by two-laser holography with Bi12TiO20 crystals," Appl. Opt. **48**(27), 5114–5120 (2009).
18. C. M. Vest, Holographic Interferometry, Wiley, New York (1979).
19. J. Blanco-García, J. L. Fernández, and M. Pérez-Amor, "Fringe localization control in holographic interferometry," Appl. Opt. **31**(4), 488–496 (1992).
20. H. Kogelnik, "Coupled Wave Theory for Thick Hologram Gratings," Bell Syst. Tech. J. **48**, 2909–2947 (1969).
21. A. A. Kamshilin, and M. P. Petrov, "Continuous reconstruction of holographic interferograms through anisotropic diffraction in photorefractive crystals," Opt. Commun. **53**(1), 23–26 (1985).

1. Introduction

Due to the employ of fringe pattern evaluation procedures [1–3] such as phase shifting and phase unwrapping, whole-field interferometric methods, like holography [4–6] and DSPI [7,8] (digital speckle pattern interferometry), enable fast and precise reconstruction of wavefronts as a whole with a precision up to $\lambda/100$ in cases of low optical noise [9]. The rotation-source [10,11] and the heterodyne (two-color or multi-wavelength) methods [12–14] are among the most promising interferometric whole-field techniques for surface contouring. In both cases the interference fringes result from the intersection of the studied surface with uniformly distant and parallel planes of constant elevation. The accuracy of the measurement mainly depends on the knowledge of the distance between the planes – the contour interval - and their direction in respect to a reference plane.

Recently a combination of those techniques was proposed and demonstrated through holographic recording in $Bi_{12}TiO_{20}$ (BTO) crystals [15–17]. In the optical setup two tunable diode lasers emitted at slightly different wavelengths thus generating a synthetic wavelength λ_S. In addition, both beams propagated in slightly different directions, such that the small beam misalignment $\delta\alpha$ acted as a fine adjustment of the interferogram spatial frequency. During the holographic recording in the thick BTO crystal the Bragg condition for generating high-visibility fringe patterns was achieved by properly selecting the values of $\delta\alpha$, providing contour intervals down to ~95 µm. Despite the good results of these works, their analyses are valid only for certain experimental conditions and are limited to particular surface geometries, since they do not consider important phenomena like the wavelength-dependent rotation of the constant elevation planes, or the loci of the fringe pattern formation.

A correct and complete determination of the constant elevation planes geometry is crucial for the measurement accuracy. As the measurements become finer, the accuracy requirements become more stringent, otherwise errors which are usually negligible for synthetic wavelengths of the order of few millimeters can lead to very inaccurate results when tenfold smaller synthetic wavelengths are used. In addition, an erroneous estimate of the direction of the constant elevation planes can lead to the false conclusion that an actually symmetrical surface with respect to a given direction is asymmetrical, or vice-versa. The theoretical development and the experiments with hybrid two-laser and beam misalignment setups performed in this work have revealed that the planes of constant elevation are no longer perpendicular to the bisector of the angle formed by the illuminating beam and the beam scattered by the object, a widely accepted concept in heterodyne holographic or speckle interferometry. In this work the direction and the spacing of the planes were calculated from the propagation vectors of the illuminating beams and the beam scattered by the object as a function of the illuminating beam angle α, the beam misalignment $\delta\alpha$ and the wavelengths of the interacting beams. The results of this vectorial analysis provided the information for designing and adjusting the illumination of the object in order to achieve a desired direction of the planes of constant elevation, which was successfully accomplished and confirmed by the experiments.

Another important issue of two-wavelength whole-field interferometry lies on the fact that smaller contour intervals enable the measurement of lower derivative surfaces. In this work it was experimentally observed that in these cases the fringe pattern was not formed on the object surface. Moreover, it was also observed that the interferogram generated by surfaces with slopes of different signals cannot be entirely visualized; instead, if the fringe pattern of a region, say, of a positive slope has a high visibility, the fringes of the remaining part with negative slope are not discernible, or vice-versa, suggesting that the fringe focusing was related to the direction of the propagation vectors of the illuminating beams relatively to the surface. Based on the theoretical development for fringe localization in two-exposure holography for deformation measurements [18,19], an expression describing the position of the fringe pattern with respect to the studied surface was derived as a function of the experimental parameters. The theoretical results provided very useful information on how to localize the interferogram by properly adjusting the optical system and how to manage the discrepancies between the surface and the fringe pattern positions.

Since an important part of the experiments consists of adjusting the propagations of the beams and the synthetic wavelengths in order to achieve high measurements sensitivities and good interferogram visibilities, in the whole theoretical analysis the Bragg condition for holographic recording and readout was taken into account.

2. Two-wavelength holographic recording

Preceding the theoretical analysis of Sections 2.1 and 2.2 a brief revision of the two-wavelength holographic process is presented below. Consider the interference of the reference and the object waves onto a $Bi_{12}TiO_{20}$ crystal in a two-wave mixing-like scheme. The waves originate from two diode lasers emitting at different wavelengths λ_1 and λ_2 such that $|\lambda_1 - \lambda_2| << \lambda_1$. The beams coming from the lasers have the same intensity and are coupled by a beam splitter in order to propagate nearly in the same direction. The following analysis takes into account the influence of the lasers detune and the misalignment of the beams on the generation of interference contour fringes on the object image. The waves impinging the BTO crystal can then be written as

$$R = R_0 \left\{ \exp[i(k_1 \Gamma_{R1} + \varphi_1)] + \exp[i(k_2 \Gamma_{R2} + \varphi_2)] \right\} \tag{1a}$$

$$S = S_0 \left\{ \exp[i(k_1 \Gamma_{S1} + \varphi_1)] + \exp[i(k_2 \Gamma_{S2} + \varphi_2)] \right\} \tag{1b}$$

where $k_{1,2} = 2\pi / \lambda_{1,2}$ and ϕ_1 and ϕ_2 are the phases at each laser output. $\Gamma_{S1,2}$ and $\Gamma_{R1,2}$ are respectively the optical paths of the object and the reference beams with wavelength $\lambda_{1,2}$ from the coupling beam splitter to the crystal. The distinction of $\Gamma_{S(R)1}$ from $\Gamma_{S(R)2}$ arises from the beam misalignment at the beam splitter output. From Eq. (1) the intensity of the holographic object image is given by [15]

$$\begin{aligned} I_D \propto |E_{D1}|^2 + |E_{D2}|^2 &\propto R_0^2 \eta_0 \left[1 + \chi^2 + 2|\chi| \cos(k_1 \Gamma_{S1} - k_1 \Gamma_{R1} - k_2 \Gamma_{S2} + k_2 \Gamma_{R2}) \right] \\ &= R_0^2 \eta_0 (1 + \chi^2) \left[1 + V \cos(k_1 \Gamma_{S1} - k_1 \Gamma_{R1} - k_2 \Gamma_{S2} + k_2 \Gamma_{R2}) \right] \end{aligned} \tag{2}$$

where $V \equiv 2|\chi| / (\chi^2 + 1)$ is the interferogram visibility. The factor χ takes into account the eventual off-Bragg readout, such that $0 < |\chi| < 1$, being $|\chi| = 1$ for perfect Bragg regime and $\chi = 0$ for completely off-Bragg processes [15,20]. Since the output power is the same for both lasers, V refers only to the Bragg regime degree. From the phase in the sinusoidal term of Eq. (2), one retrieves information about the object surface, the position of the constant elevation planes and their relative distances as well as the interferogram localization.

2.1 Interferogram positioning and distance between planes

The incidence of the collimated illuminating beam onto the analyzed surface impinging points A and B is shown in Fig. 1. Since the illuminating beams propagate in plane *xz* only, the analysis of Sections 2.1 and 2.2 will be restricted to this plane. The angle between the incident beam and *y*-axis is $\alpha + \delta\alpha$ for beam 1 and α for beam 2. The phase difference ϕ between A and B on the object surface is obtained from Eq. (2):

$$\varphi = k_1 \Gamma_{S1B} - k_2 \Gamma_{S2B} - k_1 \Gamma_{S1A} + k_2 \Gamma_{S2A}, \tag{3}$$

where $\Gamma_{S1(2)A}$ and $\Gamma_{S1(2)B}$ are the optical paths of the object beam at wavelength $\lambda_{1(2)}$ through A and B, respectively. In the equation above, the influence of the beams misalignment in the reference-beam arm on the fringe generation can be considered negligible. According to Fig. 1, the phases of Eq. (3) can be explicitly written as a function of the unit propagation vectors of the illuminating and the scattered beams $\hat{k}_1$, $\hat{k}_2$ and $\hat{k}$:

$$\varphi = 2\pi \left(\frac{\hat{k}_1}{\lambda_1} - \frac{\hat{k}_2}{\lambda_2} - \frac{\hat{k}}{\lambda_S} \right) . \vec{L} \tag{4}$$

where $\lambda_S \equiv \lambda_1 \lambda_2 / (\lambda_2 - \lambda_1)$ is the synthetic wavelength, which can be whether positive or negative. Vector $\vec{L}$ shown in this figure is the position vector of point *B* in respect to *A*. In the coordinate system of Fig. 1 the *y*-axis is the optical axis of the lens which forms the object image on the holographic medium, or the direction of the beams scattered by the object and captured by the lens, since its aperture is much smaller than the object-to-lens distance. The phase obtained in Eq. (4) describes the generation of contour fringes due to two-laser holography.
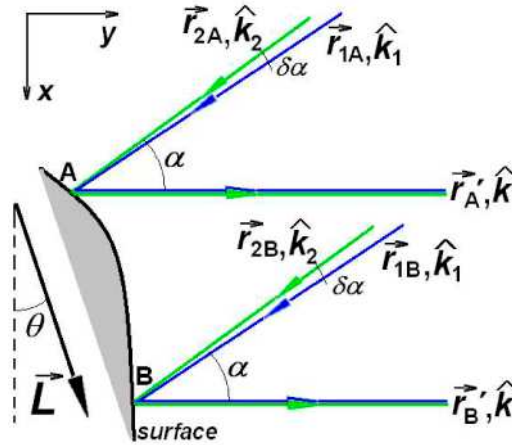

Fig. 1. Incidence of the collimated beam onto the surface.

If points A and B lay on the same plane of constant elevation (i.e., on the same bright/dark fringe), thus $\phi = 0$. According to Fig. 1, the vectors in Eq. (4) are written as $\hat{k}_1 = (\sin\alpha, -\cos\alpha)$, $\hat{k}_2 = (\sin(\alpha + \delta\alpha), -\cos(\alpha + \delta\alpha))$, $\hat{k} = (0,1)$ and $\vec{L} = L(\sin\theta, \cos\theta)$. Hence, from those vector and from Eq. (4) one obtains the direction of the elevation planes given by angle θ shown in Fig. 1:

$$tg\,\theta = \frac{\sin\alpha - \dfrac{\lambda_s\,\delta\alpha}{\lambda_2}\cos\alpha}{2\cos^2\left(\dfrac{\alpha}{2}\right) + \dfrac{\lambda_s\,\delta\alpha}{\lambda_2}\sin\alpha}, \tag{5}$$

The terms containing the synthetic wavelength show that θ depends not only on the illumination beam angle α, but also on the lasers detune $\lambda_2 - \lambda_1$, due to the misalignment angle $\delta\alpha$. Notice that when $\delta\alpha = 0$, thus $\theta = \alpha/2$, as in usual two-colour holography.

It should be emphasized that the values of the wavelengths and the angle $\delta\alpha$ cannot be set arbitrarily. Since the holographic images are obtained through volume holograms, the limits imposed by the Bragg regime must be necessarily observed and thus there must be a trade-off between all the parameters in order to obtain acceptable interferogram visibilities. Due to the beam misalignment, two phase holograms with grating vectors slightly tilted of $\delta\alpha$ with respect to each other are recorded in the BTO crystal. According to Kogelnik's coupled wave theory [20], due to this tilt and to the lasers detune the term χ in Eq. (3) is given by $\chi = \sin\xi/\xi$ for small diffraction efficiencies, where $\xi = 2\pi l_0 \sin\gamma\left[\delta\alpha/\lambda + \tan\gamma\left(n_0\lambda_s\right)^{-1}\right]$, l_0 being the interaction length of the interfering beams in the medium, 2γ the angle between them, n_0 the crystal refractive index and $\lambda = \left(\lambda_1\lambda_2\right)^{1/2}$. As mentioned in the previous section, the interferogram maximal visibility $V_{\max} = 1$ obtained in perfect Bragg processes is achieved for $\chi = 1$ and $\xi = 0$. However, the properties of the phase stepping methods for fringe evaluation allow a range of values of V smaller than 1 without introducing significant errors in the wavefront reconstruction. This tolerance for slight off-Bragg regimes can be beneficial for the wavefront analysis, since it results, if the experimental parameters are properly selected, in higher spatial frequency interferograms which in turn allow for less noisy, more sensitive and more accurate measurements [6]. As it will be seen in the following sections, the product $\lambda_s\delta\alpha/\lambda_2$ of Eq. (5) appears recurrently throughout the paper and is closely related to the Bragg condition. Through the definition of ξ above and the expansion $\chi = \sin\xi/\xi \cong 1 - \xi^2/6$, the term $\lambda_s\delta\alpha/\lambda_2$ can be written as

$$\frac{\lambda_s\,\delta\alpha}{\lambda_2} \equiv \Im \cong \frac{\sqrt{6(1-\chi)}}{2\pi\,l_0\sin\gamma}\lambda_s - \frac{\tan\gamma}{n_0} \tag{6}$$

The term $\Im$ is a key-parameter since it determines how the lasers detune and the misalignment angle must be experimentally set in order to provide desired values of contour intervals with a suitable interferogram visibility (i.e., a degree of Bragg regime).
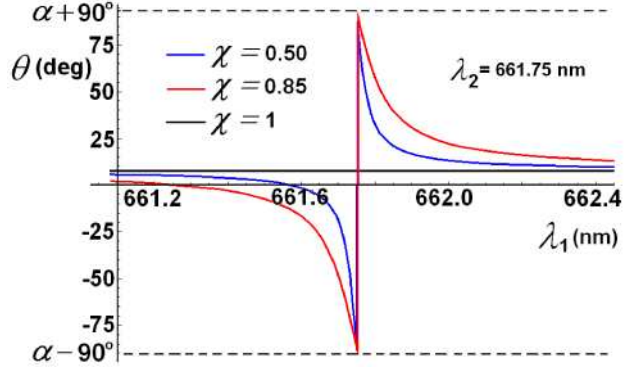
Fig. 2. Angle θ of the planes of constant elevation as a function of λ_1 for different values of χ and $\lambda_2 = 661.75$ nm.

Although θ in Eq. (5) is conveniently expressed in terms of $\Im$, a more illustrative way of displaying the dependence of θ on the lasers detune is shown in Fig. 2. In this case the wavelength of laser 2 is kept constant at 661.75 nm while the other laser is tuned. The angle θ is plotted as a function of λ_1 according to Eqs. (5) and (6) for $\chi = 1$ (black curve), $\chi = 0.85$ (red curve) and $\chi = 0.5$ (blue curve). Each curve simulates the experimental procedure through which $\delta\alpha$ is readjusted as λ_1 is changed in order to keep the same value of χ. The curves were obtained based on the parameters adopted in the experiments: the illumination angle was set to $\alpha = 0.05$ rad, the angle between the object and the reference beams inside the crystal was $2\gamma \approx 25°$, the BTO refractive index is $n_0 = 2.6$ for red light and the interaction length l_0 was estimated to be ~ 2 mm due to the tight focusing of the object image in the BTO crystal and the small area of the illuminated surfaces (not exceeding 20 cm^2). The curves show that for $\chi < 1$ the planes of constant elevation tilt rapidly so that $\theta \rightarrow \alpha \pm \pi/2$ rad as $\lambda_1 \rightarrow \lambda_2$ ($\lambda_s \rightarrow \pm\infty$). The black curve shows that when the laser beams are aligned in order to keep maximum fringe visibility throughout the process of laser detuning, the direction of the elevation planes remains constant at $\theta_0 = \arctan\left[(\sin\alpha + \tan\gamma/n_0)(2\cos^2\alpha/2 - \tan\gamma/n_0)^{-1} \right]$. From the plot, it may be also observed that if $\delta\alpha > 0$, then $\theta = 0$ only when $\lambda_1 < \lambda_2$.

The distance between two consecutive planes of constant elevation can be obtained with the help of Eq. (4). Let $\vec{R}$ be the vector representing the distance between two consecutive planes, called as sensitivity vector. Since the phase difference between them is $\phi = 2\pi$, one obtains the relation

$$\left(\frac{\hat{k}_1}{\lambda_1} - \frac{\hat{k}_2}{\lambda_2} - \frac{\hat{k}}{\lambda_s} \right).\vec{R} = 1 \tag{7}$$

Since $\vec{R} \perp \vec{L}$, from Eq. (7) the modulus of $\vec{R}$ can be given by

$$R = \left| \frac{\lambda_s}{\Im\sin(\theta-\alpha) - 2\cos\left(\frac{\alpha}{2}\right)\cos\left(\theta - \frac{\alpha}{2}\right)} \right| \tag{8}$$

The interference fringes generated on a flat surface tilted by an angle β with respect to the x-axis are obtained by determining the intersection of this surface with the planes of constant

elevation. The spatial frequency of the interferogram generated on this surface is then written as $v_S = \left|\sin\left(\theta - \beta\right)\right| / R$. The plot of v_S in Fig. 3 shows that even though $1/R$ is a minimum for $\lambda_1 = \lambda_2$, the interferogram spatial frequency increases monotonically in this region due to the factor $\left|\sin\left(\theta - \beta\right)\right|$, showing that not only the distance between the planes of constant elevation but also the wavelength-dependent rotation of these planes are responsible for the spatial frequency of the contour interferogram. In the figure, $\beta = 0$, $\lambda_2 = 661.75$ nm and $\chi = 0.98$. The spatial frequency is zero if λ_1 assumes the value $\lambda_{1\min} = \lambda_2 \left(\delta\alpha / \tan\alpha + 1\right)^{-1}$, which corresponds to $\theta = 0$ in Eq. (5).
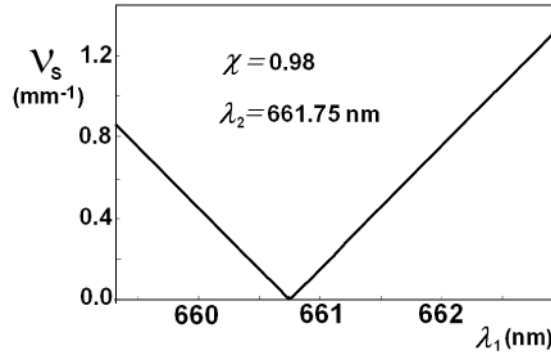

Fig. 3. Dependence of v_S as a function of λ_1, for $\beta = 0$, $\lambda_2 = 661.75$ nm and $\chi = 0.98$.

2.2 Interferogram localization

For convenience a new coordinate system was chosen with axes x' and y' perpendicular and parallel to the sensitivity vector $\vec{R}$, respectively. This choice lies on the fact that the interferogram intensity at a point P on the object can be attributed to its phase with respect to a point O on a reference elevation plane. Both points define the vector $\vec{H}$, parallel to the sensitivity vector. As usual in fringe pattern localization, it is assumed that the interferogram is not formed on the object surface, but in other region of the space. Consider points P and O as having coordinates (x', H) and $(x', 0)$, respectively, and a point Q of coordinates (X', Y') belonging to the region where the fringe pattern is formed. The total optical wave at Q is the contribution from the waves scattered by the points at the vicinity of P, as shown in the insert of Fig. 4. This region surrounding P is the base of a cone with the apex at Q. The area of the base is directly proportional to the optical aperture of the image acquisition system. The condition for fringe formation at point Q requires that the fringe visibility is a maximum, which implies that the phase variation at this point is a minimum, leading to $\partial\delta / \partial x' = 0$ [18].
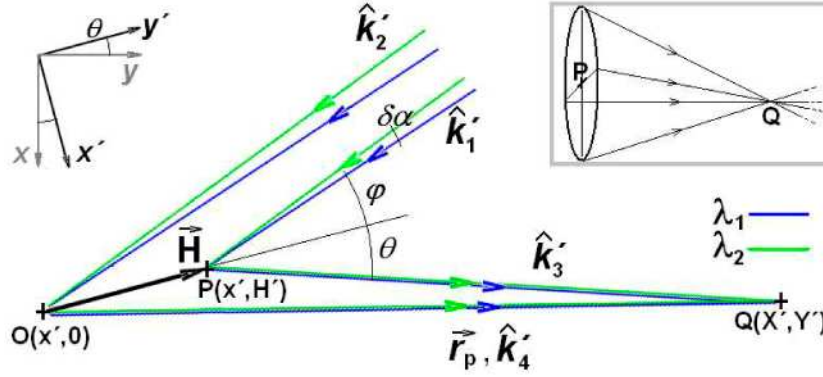
Fig. 4. Scheme of incident collimated beams and beams scattered by the surface at point P.

The phase at Q is determined analogously as in the previous section according to the scheme of Fig. 4:

$$\delta = 2\pi\left(\frac{\hat{k}_2}{\lambda_2} - \frac{\hat{k}_1}{\lambda_1} - \frac{\hat{k}_3}{\lambda_S}\right).\vec{H} + \frac{2\pi}{\lambda_S}\left(\hat{k}_3 - \hat{k}_4\right).\vec{r}_P \qquad (9)$$

where $\vec{H}$ ($\parallel \vec{R}$) is the position vector of P relatively to O, $\hat{k}_1$ and $\hat{k}_2$ are the propagation vectors of the illuminating beams, $\hat{k}_3$ and $\hat{k}_4$ are the propagation vectors of the scattered beams (see Fig. 4), and $\vec{r}_p$ the position vector of Q relatively to P. Considering a small incidence angle α of the illuminating beam onto the object surface (as in the experimental setup), and since $\hat{k}_3 - \hat{k}_4$ and $\vec{r}_p$ are nearly orthogonal, the second term in the right-hand side of Eq. (9) can be neglected, so that δ can be simplified as

$$\delta \cong 2\pi\left(\frac{\hat{k}_2}{\lambda_2} - \frac{\hat{k}_1}{\lambda_1} - \frac{\hat{k}_3}{\lambda_S}\right).\vec{H} \qquad (10)$$

In the new coordinate system, the position vector $\vec{H}$ and the normalized propagation vectors are written as $\vec{H} = (0, H)$, $\hat{k}_1 = \left(\sin\phi, -\cos\phi\right)$, $\hat{k}_2 = \left(\sin(\phi + \delta\alpha), -\cos(\phi + \delta\alpha)\right)$ and $\hat{k}_3 = \dfrac{(X'-x', Y'-H)}{\kappa} = \left(\sin\theta, \cos\theta\right)$, where $\kappa \equiv \sqrt{(X'-x')^2 + (Y'-H)^2}$, $\phi = \alpha - \theta$ and $H = H(x')$. By using the vectors above and after some algebraic manipulation the position Y' where the fringe pattern is formed can be obtained from Eq. (10) as

$$Y' = \left\{1 + \frac{\dfrac{\sin 2\theta}{2}\left(\sin\theta\dfrac{\partial H}{\partial x'} - \cos\theta\right)}{\left[\Im\sin(\alpha - \theta) + 2\cos\left(\dfrac{\alpha}{2}\right)\cos\left(\theta - \dfrac{\alpha}{2}\right)\right]\dfrac{\partial H}{\partial x'}}\right\} H(x') \qquad (11)$$

Equation (11) enables a semi-quantitative description of the fringe focusing phenomenon, since it does not provide the absolute interferogram position, but its relative position with respect to the surface. When the expression in the brackets equals 1, the fringe pattern occurs right on the object surface described by function $H(x')$. As the expression in the brackets assumes values smaller than 1, the fringe pattern is formed behind the object; otherwise, the interferogram is formed between the object surface and the imaging lens. The relation

between the slope $\partial H/\partial x'$ of the studied surface and the illumination angle α strongly influences the signal of the right-hand term in the bracket and thus it determines whether the fringes are formed behind or in front of the surface. Since the propagation vectors of all the beams in the optical setup belong to the $x'y'$-plane, the dependence of the Y-coordinates on the z-direction was not taken into account.

In typical experimental conditions, the illumination angle α is small and positive, so that $\left|\Im \sin(\alpha - \theta)\right| << 1$; if $\partial H/\partial x' > 0$, then $Y' < H(x')$, and the fringe pattern is formed behind the surface; if $\partial H/\partial x' < 0$, one gets $Y' > H(x')$, and the interferogram is localized between the object and the imaging lens. From Eq. (11) one also concludes that a decrease of the surface derivative corresponds to an increase of the distance between the object and the interferogram surfaces, to the limit for which the distance between the interferogram and the object surface tends to infinity as $\left|\partial H/\partial x'\right| \to 0$.

The influence of the illumination angles on the distance between the fringe pattern and the object surface was considered by studying the formation of the interferogram on a simple surface constituted by two concurrent planes. The intersection of this surface with $x'y'$-plane is "V"-shaped, so that $H(x')$ in this plane is given by

$$\begin{cases} H(x') = mx' + b, \text{for } x' < 0 \\ H(x') = -mx' + b, \text{for } x' < 0 \end{cases} \quad \text{where} \quad m(= \partial H/\partial x') \text{ and } b \text{ are real and positive.}$$

Figure 5 shows the surface (black curve, $m = 0.35$ and $b = 20$ mm) and the region Y' where the interferogram can be focused for $\alpha = 0.01$ rad (blue curve), $\alpha = 0.05$ rad (red curve). This figure evidences how the position of fringe focusing depends on the illumination angle and that the fringes are formed behind or in front of the surface according to its slope.
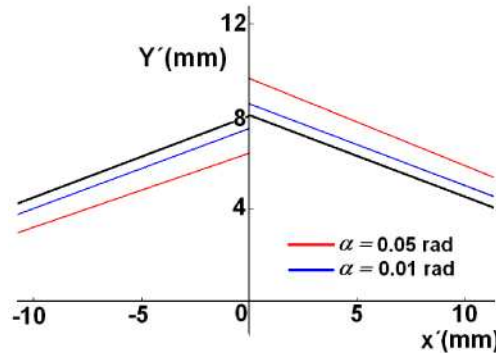

Fig. 5. Position Y' of the interference pattern for $\alpha = 0.01$ rad (blue), $\alpha = 0.05$ rad (red) with respect to the edged surface (black).

For some combinations of beam misalignment and lasers detune it is possible in principle to observe subtle changes in the fringe pattern position relatively to the object surface. This change can be noticed through a small decrease of the interferogram visibility as $\Im$ is changed. According to Eq. (11), as $|\Im|$ increases, the distance between the fringe pattern and the object surface also increases. This difference becomes more pronounced as the surface derivatives $\partial H/\partial x'$ become smaller. Figure 6(a) illustrates the behavior of Y'/H by varying the wavelength λ_1, taking $\lambda_2 = 661.75$ nm and for different values of χ. All the curves were obtained for $\partial H/\partial x' = -0.04$. The curves evidence clearly that the influence of λ_1 on the fringe position becomes more pronounced as $\lambda_1 \to \lambda_2$, i.e., for larger values of λ_S and $\Im$. Analogously as performed in Fig. 2, the black ($\chi = 1$), the blue ($\chi = 0.9$) and the red

($\chi = 0.5$) curves describe the situation in which the beams are aligned as $\left|\lambda_1 - \lambda_2\right|$ varies in order to keep the same fringe visibility. As $\left|\lambda_1 - \lambda_2\right|$ increases the values of Y'/H for all the visibilities converge to same value obtained through Eq. (11) for $\Im = -\tan\gamma/n_0$. For lower derivatives the curves present essentially the same behavior, but the relative distances increase, as shown in Fig. 6(b) for $\partial H/\partial x' = -0.012$. In any case, by examining the curves it can be noticed that the lasers detune and the beam misalignment do not produce easily observable and/or relevant changes in the fringe pattern position; both plots show that the variation of the interferogram position is larger for wavelength changes in the region of larger synthetic wavelengths (i.e., smaller spatial frequencies), and that this variation is more pronounced for lower surface derivatives. However, the interferogram generated by low-derivative surfaces cannot be easily visualized in the limit of very large synthetic wavelengths, since the intensity distribution of the resulting holographic image tends to be spatially uniform in these cases.
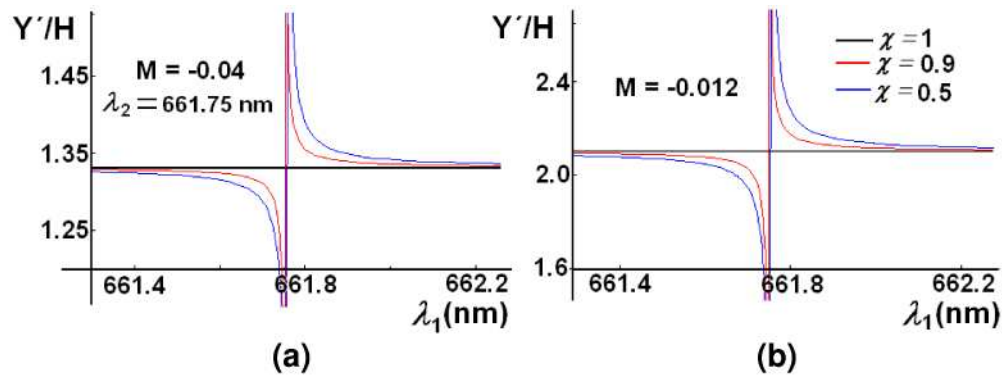

Fig. 6. Y'/H as a function of the wavelength λ_1, with λ_2=661.75 nm and $\chi = 1$, 0.9 and 0.5, for a - $M = \partial H/\partial x' = -0.04$ and b - $\partial H/\partial x' = -0.012$.

3. Experiments and results

3.1 Experimental setup

Two 30-mW diode lasers with emission centered at ~ 662 nm were employed in the holographic setup. The holographic recording occurred in the pure diffusion regime and the photorefractive BTO crystal was cut in the [110] transverse electrooptic configuration in order to take advantage from its anisotropic diffraction properties [21] for low-noise imaging with a CCD camera. The other BTO output was used for spectrum measurement by a spectrum analyser with a 600-lines/mm diffraction grating. The piezoelectrically driven mirror M1 allowed adjusting the misalignment angle with $\pm\ 10^{-5}$ rad of uncertainty. The object was mounted on a goniometer and could be rotated by angles with uncertainty $\pm 9 \times 10^{-3}$ rad. The experimental setup is shown in Fig. 7.
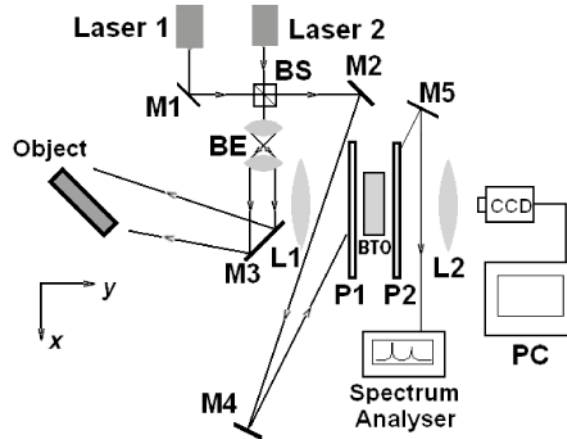
Fig. 7. Experimental setup: M1 to M5, mirrors, L1 and L2, lenses, BE, beam expander, P1 and P2, polarizers, BS, beam splitter, BTO, $Bi_{12}TiO_{20}$ crystal, CCD, camera, PC, computer.

Both lasers were tuned upon varying the current injected by the power supply. The values of λ_1 ranged from 661.80 to 663.70 nm, while λ_2 ranged from 660.55 to 662.75 nm, all values with uncertainties of ± 0.05 nm. During the laser tuning the currents of the power supply were selected in order to achieve a laser emission without mode hoping. This assured a negligible variation of the synthetic wavelength throughout the experiments. The fact that $\lambda_1 > \lambda_2$ in the whole voltage range is an experimental limitation which influences the analysis of the constant elevation planes direction.

3.2 Direction of constant elevation planes

Since λ_S is always negative due to the behavior of λ_1 and λ_2 mentioned above, one comes to the conclusion that $\delta\alpha$ must be whether null or positive in order to fulfil Eq. (6) and provide visible interferograms. This limits the flexibility in the beam alignment. In order to illustrate the consequences of this limitation, the requirements through which the constant elevation planes are parallel to the *xz*-plane in Fig. 1 are analysed. This is a very desirable configuration, remarkably in the study of surface geometries which present symmetry relatively to the *y*-axis, e.g. spherical or cylindrical surfaces. In this case, since $\bar{L}$ must be parallel to the *x*-axis, and since $\hat{k}/\lambda_S$ is perpendicular to it, the planes will have the desired direction if the vector $\Delta\hat{k} \equiv \hat{k}_1/\lambda_1 - \hat{k}_2/\lambda_2$ is parallel to the *y*-axis. By using the unit vectors $\hat{k}_1$ and $\hat{k}_2$ from Eq. (10), this condition is fulfilled when $\Im = \tan\alpha$.
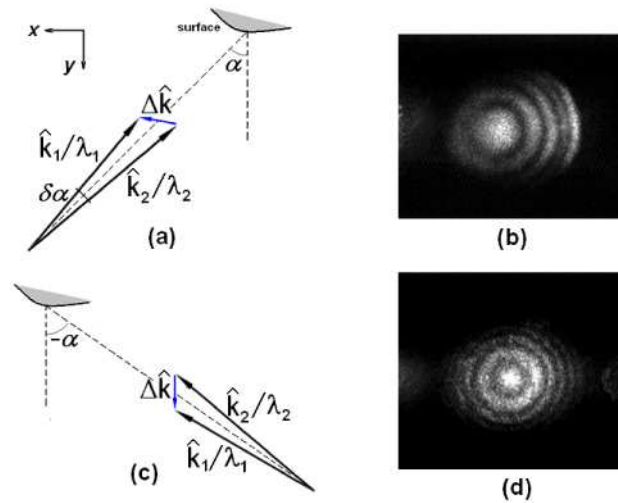
Fig. 8. a - Illumination scheme for $\alpha > 0$ showing the vector $\Delta \vec{k}$; b - contour interferogram of the surface obtained with positive α, showing excentrical contour fringes; c - illumination scheme for $\alpha < 0$; d – resulting contour interferogram of the surface with circular concentric fringes.

The illumination scheme of Fig. 8(a) (for which $\Im < 0$ and $\alpha > 0$) does not provide the desired plane direction unless $\lambda_2 > \lambda_1$ - which cannot be achieved through laser tuning – or $\delta\alpha < 0$ - which would spoil the fringe visibility according to Eq. (6). Figure 8(b) shows the contour interferogram of this surface obtained with an illumination angle $\alpha = 0.037$ rad and a synthetic wavelength $\lambda_S = -520$ μm. The excentrical contour fringes clearly evidence that the interferogram was a result of the intersection of the surface with elevation planes tilted with respect to x-axis ($\theta \neq 0$). This interferogram asymmetry cannot be removed by laser tuning or further beam alignment without the expense of a strong decrease of the fringe visibility.

In the arrangement of Fig. 8(a) the signal of illumination angle was inverted with respect to the y-axis, while the relative angular positions of vectors $\hat{k}_1$ and $\hat{k}_2$ remained unchanged. Notice that the illumination schemes of Figs. 8(a) and 8(c) are not symmetrical. In this second case it becomes clear that for certain values of λ_1 and λ_2 the vector $\hat{k}_1/\lambda_1 - \hat{k}_2/\lambda_2$ can be made parallel to the y-axis, as evidenced by the circular and concentric contour fringes of the same spherical surface as seen in Fig. 8(d).

A flat plate tilted by $\beta = 0.191$ rad (10.9°) in respect to the x-axis of Fig. 1 was used to investigate the dependence of the interferogram spatial frequency v_S on the wavelengths λ_1 and λ_2. In this study λ_2 was kept constant at 661.40 nm and the spatial frequency of the resulting straight and parallel contour fringes was measured as λ_1 was varied from 661.80 nm to 663.50 nm. For each selected value of λ_1 the beam misalignment $\delta\alpha$ was adjusted in order to provide the maximal interferogram visibility. The measured values of v_S are shown in Fig. 9, where the solid curve is the fitting of the experimental data with the expected values obtained from the expression for v_S by taking $\chi = 1$. Due to the small values of θ_0 and α, v_S can be simplified as $v_S \cong 2\sin(\theta_0 - \beta)(\lambda_1 - \lambda_2)/(\lambda_1\lambda_2)$ in a very good degree of approximation. From the fitting curve the experimental angle θ_0 between the planes of constant elevation and the x-axis for maximal fringe visibility was determined to be $\theta_{oEXP} = 0.096$ rad (or 5.5°). By taking $\alpha = 0.081$ rad, $\gamma = 0.22$ rad and $n_0 = 2.6$, the expected value of this angle was calculated to be $\theta_{oTEO} = 0.083$ rad (= 4.8°) through the expression for θ_0 in Section 2.1, showing a fairly good agreement with the value obtained experimentally. Notice

that under the influence of the misalignment angle and the laser detune the results for θ_o became significantly different from $\alpha/2 = 4 \times 10^{-2}$ rad, which is the expected value for θ in two-colour holographic interferometry .
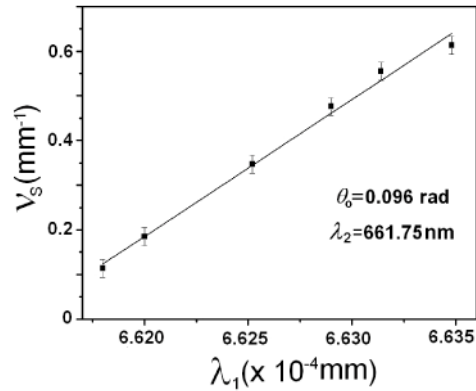

Fig. 9. Measured values of the interferogram spatial frequency v_S with maximal visibility as a function of λ_1, for $\lambda_2 = 661.4$ nm. The solid curve is the fitting of the experimental data with the theoretical expression of v_S.

3.3 Fringe pattern localization

The two-laser holographic imaging of the surface constituted of two concurrent planes described in Section 2.2 was performed in order to verify the predictions of that section based on Eq. (11). The images of the object shown in Fig. 10 confirm those predictions. In Fig. 10(a), when the left half ($x' > 0$ and $\partial H / \partial x' < 0$, according to the coordinate system of Fig. 4) of the interferogram was focused, the fringe pattern in the right side of the object (for which $\partial H / \partial x' > 0$) appears completely blurred. Figure 11(b) focuses the right half of the interferogram of the same object; as expected, in this case the contour fringes of the left half cannot be discerned. Figures 10(c) and 10(d) illustrate the same phenomenon by imaging a 37-mm radius-of-curvature spherical surface. For both figures, $\lambda_S = -420$ μm, $\delta\alpha = 2.1 \times 10^{-4}$ rad and $\alpha = 5 \times 10^{-2}$ rad.
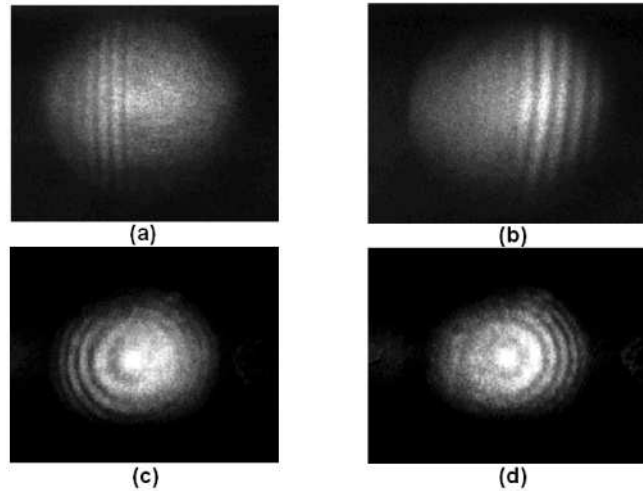
Fig. 10. Two-wavelength holographic imaging of the edge-shaped surface by focusing the fringe pattern of a –the left half ($x' > 0$ and $\partial H/\partial x' < 0$) of the surface, and b - the right half of the surface ($x' < 0$ and $\partial H/\partial x' > 0$); two-wavelength holographic imaging of the spherical surface by focusing the fringe pattern of c – the left and d – the right sides of the surface.

As predicted by Eq. (11), for $\theta = 0$ one gets $Y' = H$, and thus the fringe pattern is formed on the surface and can be integrally visualized in a single exposure regardless the surface slope and the laser detune. In order to verify this prediction the contour interferogram of the same object was studied under the same value of $\Im$ and with the illumination angle α set at negative values in order to obtain null values of θ, as described in the previous section. Figure 11 shows the resulting contour fringe pattern with the arrow indicating the edge position which separates the negative slope from the positive slope of the surface. As expected from Eq. (11), by using this illumination angle, good-visibility fringes can be clearly visualized along both sides of the surface. The aperture of the optical system was the same as that used in Fig. 10. Notice that in Fig. 8(d) for which $\theta = 0$ the interferogram resulted from a surface with positive and negative slopes was also integrally obtained.
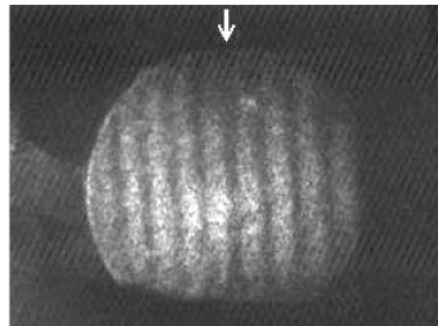

Fig. 11. Contour fringe pattern of the whole edge-shaped surface achieved for $\theta = 0$. The arrow separates the negative from the positive slope of the surface.

The dependence of the fringe position on the surface derivative was also investigated in deeper detail. For this purpose the loci of various contour fringe patterns of a flat plate were measured as its inclination (i.e., surface derivative $\partial H/\partial x'$) around the z-axis in Fig. 4 was

progressively varied. For each plate inclination, the CCD camera was positioned in order to achieve the best possible visibility of the fringe pattern. Then a reticule pattern serving as a focusing reference was positioned between the object and lens L1 and was displaced along the *y*-axis. The position of the reticule pattern with respect to the object for which both the reticule and the interferogram were sharply imaged by the optical system was considered as the interferogram position Y'. By setting the experimental parameters on $\lambda_1 = 662.60$ nm, $\lambda_2 = 661.70$ nm, $\alpha = 5 \times 10^{-2}$ rad and $\delta\alpha = 5.5 \times 10^{-4}$ rad, the fringe positions were measured for different surface inclinations and fitted to the Y-values (solid curve) given by Eq. (11), as shown in Fig. 12. Through the error bars a certain degree of subjectivity in the determination of the interferogram visibility was taken into account. A *H*-independent term was phenomenologically added to the fitting function since the measurement obtained absolut values of Y'. This term was determined to be 21.9 mm. The plot of Fig. 12 shows the good agreement of the experimental results with the theoretically predicted ones. The discrepancy between the theoretical curve and the measured data for higher surface inclinations can be mainly attributed to the approximation of Eq. (10), which requires the unit vectors $\hat{\tilde{k}}_3$ and $\hat{\tilde{k}}_4$ to be nearly parallel. As the modulus of the surface derivative increases, the fringe pattern is formed closer to the object surface and the difference $\hat{\tilde{k}}_3 - \hat{\tilde{k}}_4$ becomes not negligible, so that Eqs. (10) and (11) tend to be no longer valid. Moreover, the determination of the focused interferogram by visual means may induce to errors, remarkably in a derivative region in which the changes in the fringe position become more subtle.
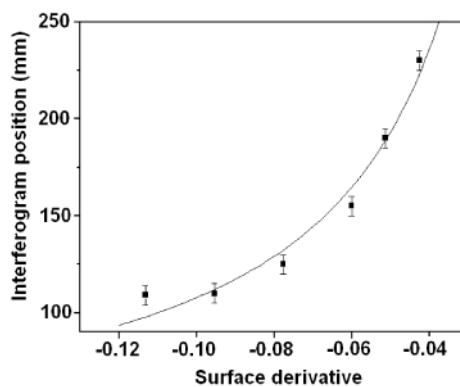

Fig. 12. Measured loci of the contour interferogram generated by a flat plate as a function of its inclination.

4. Conclusions

It has been evidenced the remarkable influence of the beams misalignment and the wavelength detune in surface contouring by whole-filed interferometry with thick holographic media. The proper knowledge of these parameters strongly contributes to the accuracy and precision of wavefront reconstruction. Derived from the coupled wave theory for thick gratings an expression relating the misalignment, the synthetic wavelength and the beam illumination angle was obtained, providing information on how to adjust those parameters in order to obtain desired combinations of interferograms visibility and spatial frequency.

The spatial frequency of the fringe pattern with visibility smaller than unit depends on the interacting wavelengths and the beams misalignment in two ways, through the rotation of the constant elevation planes with respect to the studied surface and through the variation of the distance between the planes. For a given synthetic wavelength, the beam misalignment can

be adjusted in order to provide perfect Bragg regimes, resulting in maximal fringe visibilities. In this case, it was both theoretically and experimentally demonstrated that the direction of the constant elevation planes depends exclusively on parameters related to the holographic medium and the geometry of the optical setup. For this reason the direction of the planes can significantly differ from the results expected for two-wavelength processes with no beams misalignment.

According to the theoretical and the experimental results the fringe pattern position can be mainly determined as a function of the slope of the studied surface and its position relatively to the illuminating beam. Contour fringe patterns can be significantly formed apart from the studied surface, depending on its slope in respect to the x'-axis, so that the lower the surface derivative, the more distant the interferogram from the surface. The signal of the illuminating beam angle in respect to the surface (or to the coordinate system) determines whether the fringe pattern is formed in front of or behind the surface. All this information can be useful for fringe obtaining during the process of laser tuning and beam alignment. The theoretical developments have shown that the laser tuning does not appreciably change the position of the interferogram. Indeed, in the experiments only very small and barely measurable changes in the fringe pattern visibility were observed as a function of the wavelength detune.

The configuration for which the planes of constant elevation are parallel to the xz-plane ($\theta = 0$) was found to be particularly interesting and was achieved by properly arranging the illuminating beams and selecting the interacting wavelengths. It was demonstrated that the limitation of focusing the whole contour interferogram of a surface with slopes of different signals can be overcome by getting $\theta = 0$, since in this case the fringe pattern is formed on the surface, regardless its geometry. This configuration is also useful remarkably for visual inspection and for the investigation of rather complex, multiple slopes, free-form objects. When the studied object is symmetric relatively to the y-axis, the resulting interferogram is also symmetric, thus enabling a more intuitive qualitative evaluation of the surface shape.

Acknowledgements